Crystal structure, magnetic and optical investigation, Hirshfeld surface analysis, and DFT calculation of new organic-inorganic hybrid (NH3(CH2)2CO2H)2[MnCl4(OH2)2]

Abdellah Kaiba, Mohammed H. Geesi, Philippe Guionneau

Crystal structure, magnetic and optical investigation, Hirshfeld surface analysis, and DFT calculation of new organic-inorganic hybrid (NH3(CH2)2CO2H)2[MnCl4(OH2)2]

Abdellah Kaiba, Mohammed H. Geesi, Philippe Guionneau

Crystal structure, magnetic and optical investigation, Hirshfeld surface analysis, and DFT calculation of new organic-inorganic hybrid $(NH_3(CH_2)_2CO_2H)_2[MnCl_4(OH_2)_2]$

A. Kaiba [a,*], Mohammed H. Geesi [b], P. Guionneau [c]

[a] Department of Physics, College of Science and Humanities in Al-Kharj, Prince Sattam Bin Abdulaziz University, Al-Kharj, 11942, Saudi Arabia
[b] Department of Chemistry, College of Science and Humanities in Al-Kharj, Prince Sattam Bin Abdulaziz University, Al-Kharj, 11942, Saudi Arabia
[c] CNRS, Univ. Bordeaux, Bordeaux INP, ICMCB, UMR 5026, 87 Av. Dr A. Schweitzer, F-33600, Pessac, France

ARTICLE INFO

Keywords:
XRD
Micro-Raman spectroscopy
XPS
VSM
DFT calculation

ABSTRACT

A novel hybrid material, blending organic and inorganic components $(NH_3(CH_2)_2CO_2H)_2$ $[MnCl_4(OH_2)_2]$, has been successfully synthesized and meticulously examined. This intriguing compound crystalizes in monoclinic system, with *C*2/*c* space group. The unit cell dimensions are as follows: a = 21.497 (8) Å, b = 7.212 (2) Å, c = 11.149 Å, β = 109.09 (2)°, with a unit cell containing four entities (Z = 4). The asymmetric unit consisted of a combination of one half of $½[Cl_4Mn(OH_2)_2]^{2-}$ and an organic $^{+}NH_3(CH_2)_2CO_2H$ cation. The structural integrity is upheld through an intricate three-dimensional hydrogen network, serving as a stabilizing force for the crystal lattice.

Notably, the resolved structure unveils a stratified arrangement along the b-axis, creating distinct layers within the material, separating the organic and inorganic components. The intricate interplay of intermolecular forces, specifically involving H···Cl, O···O, and H···H interactions, has been thoroughly examined using Hirschfeld surface analysis. Furthermore, we employed Density Functional Theory (DFT) calculations to optimize the molecular structure.

To gain deeper insights into its properties, we conducted micro-Raman spectroscopy measurements to elucidate the vibration modes exhibited by the compound. Additionally, the material's characteristics were probed using a Vibrating Sample Magnetometer (VSM), the compound exhibits ferromagnetism. The UV–visible absorbance spectroscopy, providing comprehensive information about its optical properties (energy gap is about 4.0 eV).

1. Introduction

In recent years, hybrid-like perovskites have garnered significant attention within the scientific community due to their remarkable physical properties. These compounds belong to a unique semiconductor family that exhibits exceptional optoelectronic characteristics, making them promising candidates for applications in photovoltaic (PV) devices and light-emitting diodes (LEDs) [1–3]. What sets these materials apart is their ability to combine the desirable features of both inorganic and organic components into a single hybrid compound.

Within this intriguing family, researchers can harness the electronic properties, robust thermal stability, and luminescent efficiency inherent to inorganic sub-networks. Simultaneously, they can take advantage of the structural versatility and flexibility offered by organic sub-networks [4–8]. It's important to note that the hybrid nature of these materials not only allows for the combination of organic and inorganic properties but also holds the potential to yield entirely new properties through synergistic interactions.

The perovskite AMX_3 family has been extensively investigated for over 80 years. In this notation, 'A' represents the organic cation, 'M' can include elements like Fe^{2+}, $Cu^{2+,}$ Co^{2+}, Cr^{2+}, Sn^{2+}, or Mn^{2+}, and 'X' denotes a halogen atom. Researchers have conducted comprehensive studies on their magnetic, electrical, optoelectronic (both photo- and electroluminescence), and nonlinear optical characteristics [9–15].

These hybrid perovskites provide a unique opportunity to combine the advantageous traits of organic and inorganic components at a

* Corresponding author.
E-mail address: a.kaiba@psau.edu.sa (A. Kaiba).

Table 1
Crystal structure data refinement.

Empirical formula	C6 H20 Cl4 Mn N2 O6
Formula weight	412.98
Temperature	293 (2) K
Crystal system	Monoclinic
Space group	C 2/c
Unit cell dimensions	a = 21.497 Å b = 7.212 Å c = 11.149 Å β = 109.09°.
Volume	1633.5 Å^3
Z	4
Density (calculated)	1.679 Mg/m^3
Absorption coefficient	1.481 mm^{-1}
F (000)	844
Theta range for data collection	3.385–27.621°.
Index ranges	−27 ≤ h<=27, −9 ≤ k<=9, −14 ≤ l<=14
Reflections collected	3330
Independent reflections	1862 (R_{int} = 0.0208)
Data/restraints/parameters	1862/2/80
Goodness-of-fit on F^2	1.027
Final R indices [I > 2 sigma(I)]	R_1 (0.0384), wR_2 (0.1093)
R indices (all data)	R_1 (0.0531), wR_2 (0.122)1
Largest diff. Peak and hole	0.515 and −0.480 e.Å^{-3}

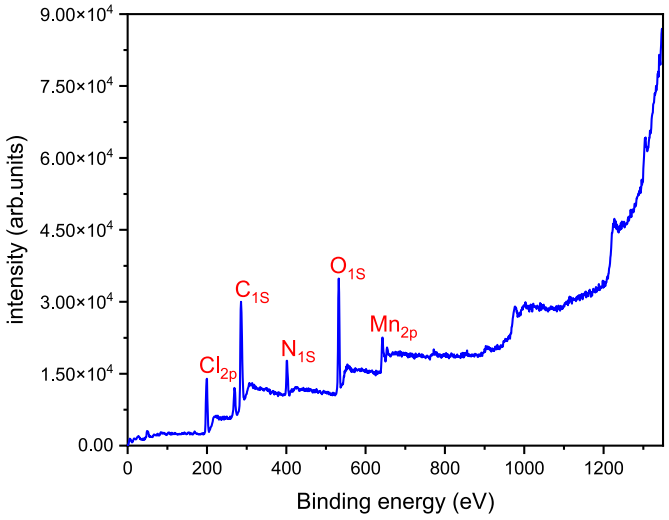

Fig. 1. The whole XPS spectrum of $C_6H_{20}Cl_4MnN_2O_6$.

molecular scale, forming a single crystalline composite. Most of these systems exhibit perovskite-type structures, with inorganic layers composed of octahedral anion (MX_6) or tetrahedral anion (MX_4) coordinated elements, such as zinc and cobalt. The organic cation's ammonium group NH3 plays a crucial role in connecting the organic molecule to the halogen X through hydrogen bonds, ensuring the cohesion of the molecular crystal. This linkage can occur in two distinct configurations: one hydrogen atom bridging the halide while two hydrogens attached to the terminal halogens (terminal halogen configuration), or vice versa, with two bridging and terminal hydrogens, as seen in the case of cobalt metal. Previous studies have also explored composites involving amino acids instead of monoamine or diamine ligands [16–20].

Understanding and controlling these structures are pivotal for tailoring their physical properties, both for fundamental research and prospective applications. The thermal, magnetic, electrical, and optical attributes of these materials hold significant promise for various technological applications, especially within the realm of solar energy storage and photovoltaic cells [21–26]. Notably, the most efficient of these materials to date employ lead as the metal, monoamines ligand, and iodine [21–23,27–30]. However, these materials come with their own set of challenges, including environmental concerns due to the presence of lead, susceptibility to moisture-induced degradation over time, and sensitivity to oxygen. In this context, we have opted to employ β-Alanine (NH_2-$(CH_2)_2$–CO_2H) and Manganese chloride $MnCl_2$.

2. Experimental

2.1. Instrumental techniques and materials synthesis

Obtaining single crystals of the perovskite-type compound titled "$C_6H_{20}Cl_4MnN_2O_6$" was achieved through a diffusion method involving carefully prepared solutions at room temperature. The formation of this molecular crystal took place as the solutions gradually evaporated.

The process for obtaining these single crystals can be summarized as follows: First, a solution of hydrochloric acid (1 ml) (HCl) with a concentration of 37 % was utilized to protonate an aqueous solution containing the amino acid alanine $NH_2(CH_2)_2CO_2H$ (1 g, 11.2 mm l). Subsequently, this protonated solution was slowly introduced into an aqueous solution of manganese chloride (0.7 g, 5.6 mm l). The light pink homogeneous solution was formed, and after a few days at room temperature, a single crystal suitable for X-ray diffraction analysis was formed.

$$2(NH_2(CH_2)_2CO_2H{+}2HCl + MnCl_2 \rightarrow (NH_3(CH_2)_2CO_2H)_2[MnCl_4(OH_2)_2]$$

To ensure the material's purity, X-ray Photoelectron Spectroscopy (XPS) analyses were conducted using the K-Alpha XPS System. This system employs a micro-focused monochromatic Al Kα X-ray source with an energy of 1486.6 eV. Additionally, further investigation was carried out using the SENTERRA II Raman Microscope spectroscopic technique.

To evaluate the magnetic properties, a Vibrating Sample Magnetometer analysis (VSM) was performed under ambient temperature conditions. The analysis of selected single crystals was conducted using the Nonius Kappa CCD diffractometer, which is equipped with a Mo (λ = 0.71073 Å) anticathode. During the measurement process, both φ and ω scan modes were utilized, and the crystal-detector distance was set at 35 mm. The collected data was processed using the DENZO-SMN program.

2.2. Crystal structure

The crystal structure hypothesis was initially generated using the SIR 97 program [31]. Subsequently, the SHELX 97 program was employed for the comprehensive refinement of all structural parameters. This refinement utilized the well-known method of full-matrix least squares based on squared structural factor F2 [32]. It is important to mention that these software applications were included within the WINGX software suite [33].

During the refinement process, hydrogen atoms were placed theoretically and subjected to isotropic refinement. Their placement was based on geometric considerations, taking into account the typical lengths and angles of covalent bonds. The final resolution of the structural analysis resulted in a residual electronic density ranging from −0.480 to 0.515 e/Å^3. The reliability factors of the refinement demonstrate its high quality.

For the creation of graphical representations, the MERCURY software [34] was utilized. A comprehensive summary of all data can be found in Table 1. To preserve the structural data, it has been archived under the CCDC (No. CCDC 2212204). Note that all bond lengths, angles, torsion angles, and atom positions are provided in the supplementary data file.

3. Results and discussion

3.1. XPS measurement

The compound's purity was verified through XPS analysis, which

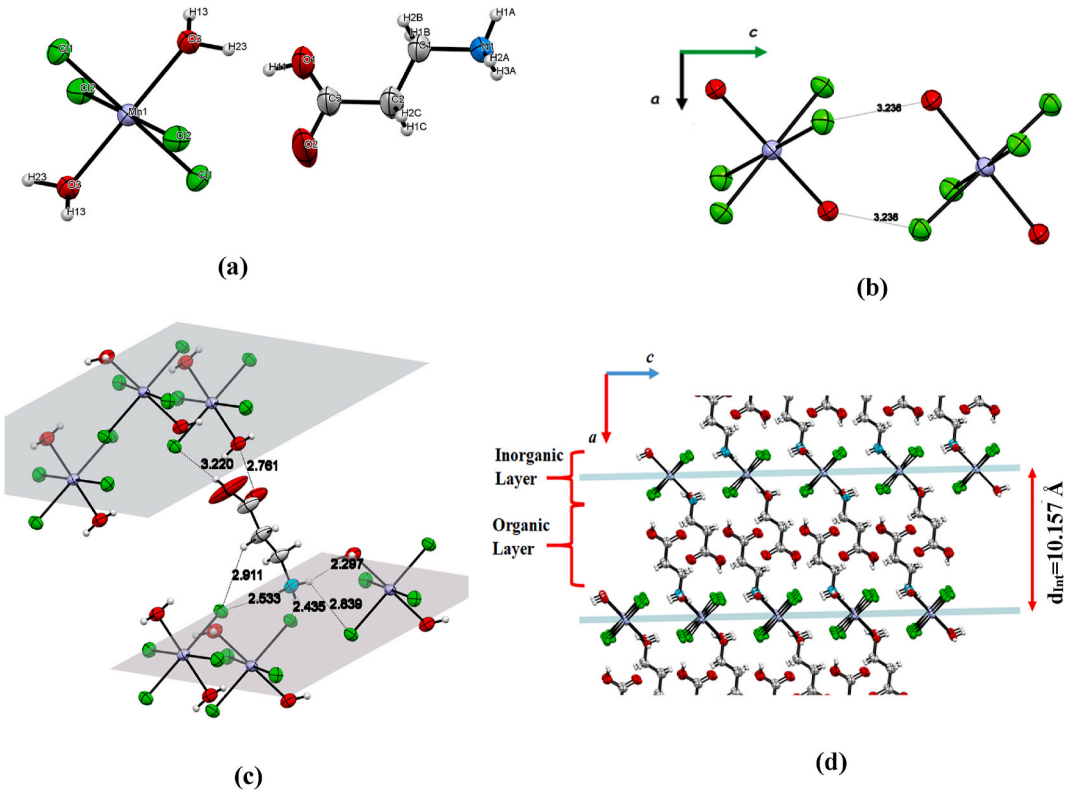

Fig. 2. **(a)** Unit asymmetric view. **(b)** Octahedron connection through hydrogen bonds (OH2···Cl) along the b-axis. **(d)** Connection between organic and inorganic sheets via *N*–H···Cl, C═O···Cl, *C*–O···OH_2, and CH···O hydrogen bonds (dashed lines). Crystal packing view along the b-axis illustrating the layered system along the a-axis.

Table 2
Hydrogen bonds length **(a)** and angles **(b)** between the unit cell and neighboring atoms of $C_6H_{20}Cl_4MnN_2O_6$.

(a)	
Hydrogen bond	Length (Å)
O_1 … ….O_3	2.767 (2)
O_2 … ….Cl_2	3.209 (4)
N_1 … ….O_3	3.143 (2)
N_1 … ….Cl_1	3.375 (3)
N_1 … ….Cl_2	3.384 (2)
N_1 … …Cl_1	3.237 (2)
N_1 … …Cl_2	3.526 (2)
(b)	
Hydrogen bonds	Angle (°)
N_1–H_{1A} … ….Cl_1	135.5 (2)
N_1–H_{1A} … ….Cl_2	124.9 (3)
N_1–H_{3A} … ….O_3	145.4 (1)
N_1–H_{3A} … ….Cl_1	127.7 (3)
N_1–H_{2A} … ….Cl_2	161.1 (1)
O1–H_{11} … ….O_3	146.6 (2)
O_3–H_{23} … …O_1	166.77
C_3–O_2 … ….Cl_2	117.6 (3)

provided conclusive evidence. The survey scan, shown in Fig. 1, clearly displays distinct peaks corresponding to the presence of manganese, chloride, oxygen, carbon, and nitrogen atoms. Specifically, significant peaks for Mn2p, Cl2p, O1s, C1s, and N1s were observed at 642 eV, 199 eV, 532 eV, 286 eV, and 402 eV, respectively. The composition analysis revealed the following percentages: 2.31 % manganese (Mn), 9.54 % chloride (Cl), 20.25 % oxygen (O), 57.53 % carbon (C), and 10.37 % nitrogen (N).

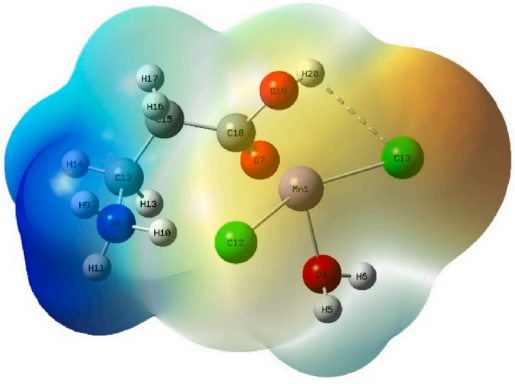

Fig. 3. Electrostatic surface potential of $C_6H_{20}Cl_4MnN_2O_6$ obtained with the DFT/B3LYP/LANL2MB method.

3.2. *X-ray diffraction investigation*

The compound exhibits a monoclinic configuration with a space group designated as *C*2/*c*. The unit cell parameters are as follows: a = 21.497 (8) Å, b = 7.212 (2) Å, c = 11.149 (2) Å, β = 109.09 (2)°, and Z = 4. Within the asymmetric unit, there are two moieties: $^{+}NH_3$-$(CH_2)_2$–COOH and one half of ½ $[Cl_4Mn(OH_2)_2]^{2-}$ (shown in Fig. 2a). Hydrogen atom placement was theoretical.

In the unit cell, there is a single organic chain of $^{+}NH_3$-$(CH_2)_2$–COOH in a trans conformation, with torsion angles approximating 180°. The Mn atom is centrally positioned with an occupation factor of 0.5, forming a trihedral coordination with four Cl atoms and two H_2O molecules. In the packing, the Mn forms isolated octahedrons $[Cl_4Mn(OH_2)_2]^{2-}$ connected via hydrogen bonds between H_2O and Chlorine

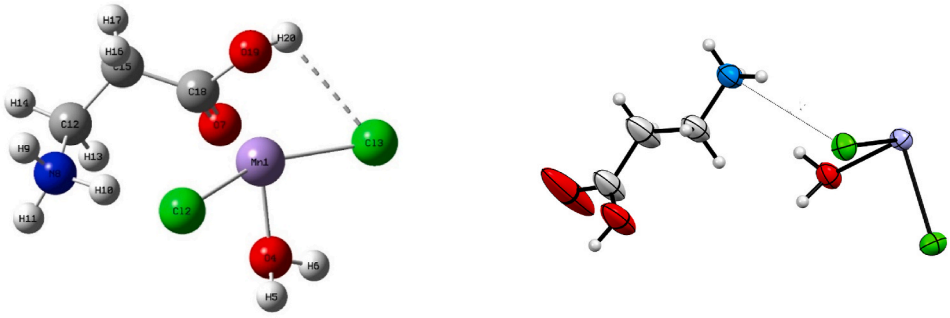

Fig. 4. Comparison of Optimized structure of $C_6H_{20}Cl_4MnN_2O_6$ calculated by the DFT/B3LYP/LANL2MB method and solved structure from X-ray diffraction.

Table 3
Comparison of theoretical and experimental **(a)** bond lengths and **(b)** angles for $C_6H_{20}Cl_4MnN_2O_6$.

(a)		
Bond length (Å)	Theoretical	experimental
Mn_1–Cl_1	2.44747	2.498 (1)
Mn_1–Cl_2	2.54108	2.551 (7)
Mn_1–O_3	1.93405	2.223 (5)
C_2–C_3	1.54289	1.485 (5)
C_1–C_2	1.5568	1.444 (4)
N_1–C_1	1.54968	1.480 (4)
C_3–O_2	1.47657	1.294 (4)
C_3–O_1	1.32589	1.178 (5)
(b)		
Angle (°)	Theoretical	experimental
Cl_1–Mn_1–O_3	151.83	90.9 (8)
O3–Mn_1–Cl_2	84.7089	85.9 (2)
Cl_1–Mn_1–Cl_2	86.2136	89.1 (3)
N_1–C_1–C_2	110.282	114.1 (6)
C_1–C_2–C_3	110.154	114.4 (6)
C_2–C_3–O_1	124.717	124.8 (2)
C_2–C_3–O_2	114.119	112.9 (8)

along the c-axis, with bond lengths around 3.236 Å (as shown in Fig. 2b). The Mn–Cl bond lengths measure approximately 2.551 Å and 2.498 Å, while the Mn–O bond length is around 2.218 Å. The bond angles around the Mn atoms range from about 85.91° to 94.04°. A calculated distortion parameter (ε = 24.08°) indicates significant distortion, deviating from 90° for the 12 cis Φ angles in the coordination sphere of the octahedron [35].

There are three types of hydrogen bonds observed: *N*–H···Cl with bond distances ranging from 2.345 Å to 2.839 Å, *N*–H···OH_2 between the NH_3 group and the H_2O of the octahedron with a bond length of approximately 2.287 Å, and OH···Cl and C═O···OH_2 involving the acid function of the $^{+}NH_3$-$(CH_2)_2$–COOH chain and the $[Cl_4Mn(OH_2)_2]^{2-}$ octahedron with bond lengths of around 3.220 Å and 2.761 Å, respectively (as shown in Table 2 and Fig. 2c).

The hybrid structure exhibits a layered architecture with alternating organic and inorganic sheets along the a-axis. The inorganic sheet consists of isolated octahedrons $[Cl_4Mn(OH_2)_2]^{2-}$, while the organic sheet is formed by $^{+}$ NH_3-(CH2)$_2$–COOH chains. The cohesion between these sheets is maintained through hydrogen bond interactions. The interlayer distance between two adjacent inorganic layers is approximately 10.157 Å (refer to Fig. 2d).

3.3. DFT calculation

DFT calculations using the Gaussian 16w program [36] were performed to optimize the molecular geometry of the compound, utilizing the unit cell parameters (a = 21.497 (8) Å, b = 7.212 (2) Å, c = 11.149 Å, β = 109.09 (2)°, and Z = 4) and atomic positions as input. The electrostatic potentials were also calculated. The computational procedures employed a combination of the B3LYP correlation functional, LANL2MB basis set, and Becke's three-parameter exchange functional [37–42]. Visualization of the results was done using Gauss View 6.1.1 software [43].

In the calculated electrostatic surface potential (ESP), the negative regions representing hydrogen bond acceptors are depicted in red, while the positive regions representing hydrogen bond donors are shown in blue. Fig. 3 visually demonstrates that the N atom of the amino acid acts as a hydrogen bond acceptor.

Fig. 4 presents a comparison between the unit cell structure obtained from X-ray diffraction and the optimized structure calculated using the DFT method for $C_6H_{20}Cl_4MnN_2O_6$. The bond lengths, bond angles, and torsion angles are compared with those obtained from the structural resolution (refer to Table 3). Notably, there is a more significant disparity observed in the inorganic part. The bond lengths vary from 0.009 Å to 0.289 Å, and the bond angles range from 0.1° to 61°.

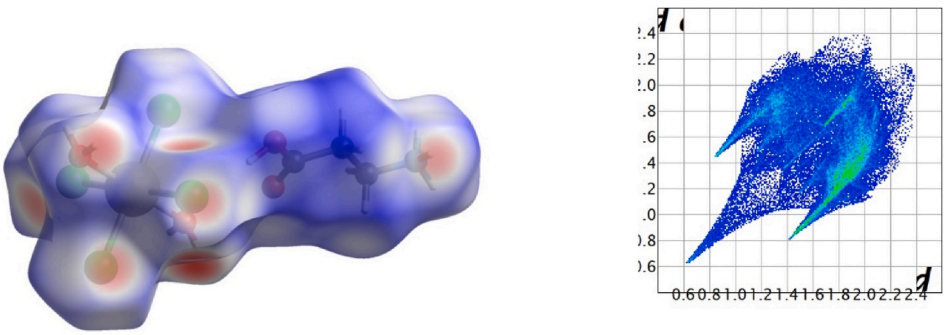

(a) **(b)**

Fig. 5. Hirshfeld surface mapped over dnorm (a) of the asymmetric unit and 2D fingerprint plot (b) for the title compound.

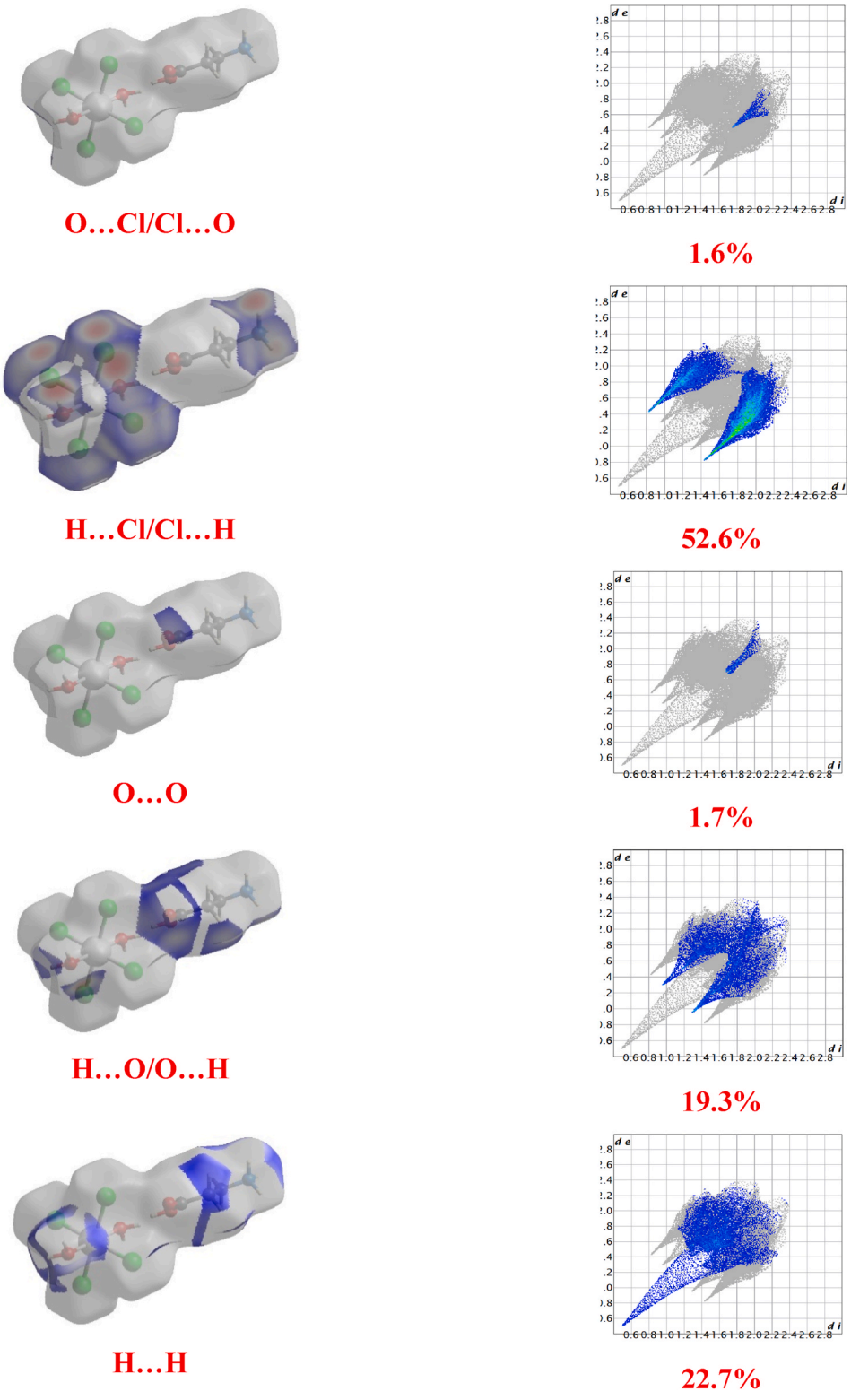

Fig. 6. 2D fingerprint plot $C_6H_{20}Cl_4MnN_2O_6$ showing contributions from different contacts.

However, the bond length and bond angle agreement is good for the organic cation. Specifically, the *C*–C bond length ranges from 1.549 Å to 1.556 Å, and the *N*–C bond length is approximately 1.542 Å. The *C*–O and C═O bond lengths are 1.476 Å and 1.325 Å, respectively. The *N*–C–C, *C*–C–C, *C*–C–O, and *C*–C═O angles in the organic chain are approximately 110.3°, 110.2°, 114.1°, and 124.7°, respectively. The torsion angles *N*–C–*C*–C, *N*–C–*C*–O, and *N*–C–C═O in the organic chain are approximately 88.6°, 43.6°, and 161.1°, respectively, indicating the deformation of the organic part.

3.4. Hirshfeld surface analysis of $C_6H_{20}Cl_4MnN_2O_6$

The crystal packing interactions were analyzed using Hirshfeld surface analysis, aided by the Crystal Explorer software [44]. Fig. 5

Table 4
Closest contacts and their percentage contributions to the Hirshfeld surface.

Type of contact	Contribution (%)
H···Cl/Cl···H	52.6 %
H···H	22.7 %
Cl···Cl	0.7 %
H···O/O···H	19.3 %
O···Cl/Cl···O	1.6 %
O···O	1.7 %
H···C/C···H	1.3 %

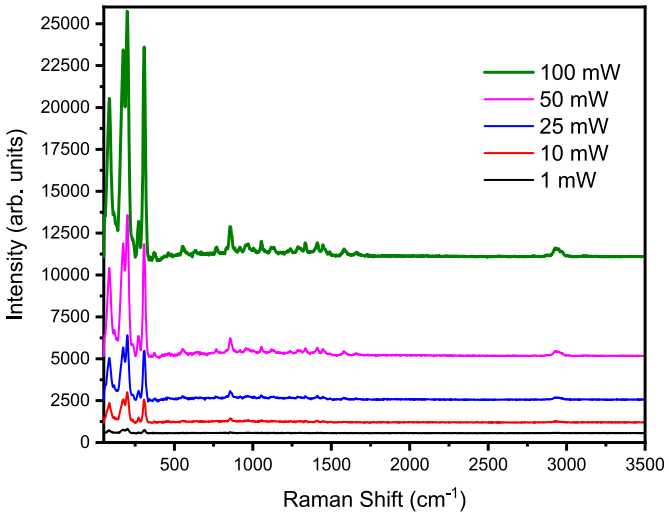

Fig. 7. Raman spectrum of $C_6H_{20}Cl_4MnN_2O_6$ obtained using a red laser with a wavelength of 532 nm at different power levels (1, 10, 25, 50, and 100 mW). (For interpretation of the references to colour in this figure legend, the reader is referred to the Web version of this article.)

illustrates the Hirshfeld surface and its d_{norm} mapping, providing insights into intermolecular contacts within the unit cell.

In Fig. 5a, the Hirshfeld surface visualization showcases different types of interactions. The red patches represent the first type, characterized by shorter distances and an abundance of *N*–H···Cl hydrogen bonds. The blue and white regions correspond to the second type, encompassing H···H, O···H, and O···O interactions. Notably, the red areas on the d_{norm} surface align with the interactions observed in the crystal structure.

To further analyze the interactions, 2D fingerprint plots were employed, emphasizing specific atom pairs and differentiating the contributions from various overlapping interactions. Fig. 5b summarizes this analysis, mapping the Hirshfeld surfaces with d_{norm} for the titled compound.

Within the crystal packing, hydrogen bonds (H···Cl) were the predominant interaction, accounting for 52.6 % of the observed interactions. H···H hydrogen bonds were the second most prevalent, contributing 22.7 % to the surface due to the presence of hydrogen atoms on the molecular surface. The longer O···O interaction contributed 1.7 % to the surface, primarily at the center of the 2D fingerprint maps. The O···H interaction constituted 19.3 % of the Hirshfeld surface. Overall, the H···Cl connection was the most dominant from a quantitative perspective, ensuring structural cohesion (refer to Fig. 6 and Table 4).

Hirshfeld surface analysis holds significant importance and promise in the field of crystal engineering as it allows for both quantitative and qualitative assessments by vividly displaying all hydrogen-bond interactions.

Table 5
Raman band assignment of $C_6H_{20}Cl_4MnN_2O_6$.

wavenumber (cm^{-1})	Assignments
175 and 200	[MnCl4(H2O)] *sym* and assym Str vib
87	[MnCl4(H2O)] binding vib
272 and 307	Mn–Cl *sym* and assym Str vib
550	Mn–O str vib
460	NH_3 twisting
663, 770 and 796	*C*–C═O, *C*–C–O def (within and out of the plane)
855	*C*–H rocking vib
954	*C*–C Str vib
969	*O*–H Str vib
156	*C*–C skeletal
1249	NH_3 def vib
1189	OH def vib
1336	-CH_2-Wagging vib
1441	-CH_2- def vib
1449 and 1489	-CH_2- *sym* and assym def vib
1580	C═O str of COOH
2926 and 2941	*sym* and assym Str vib
2951 and 3000	Str vib

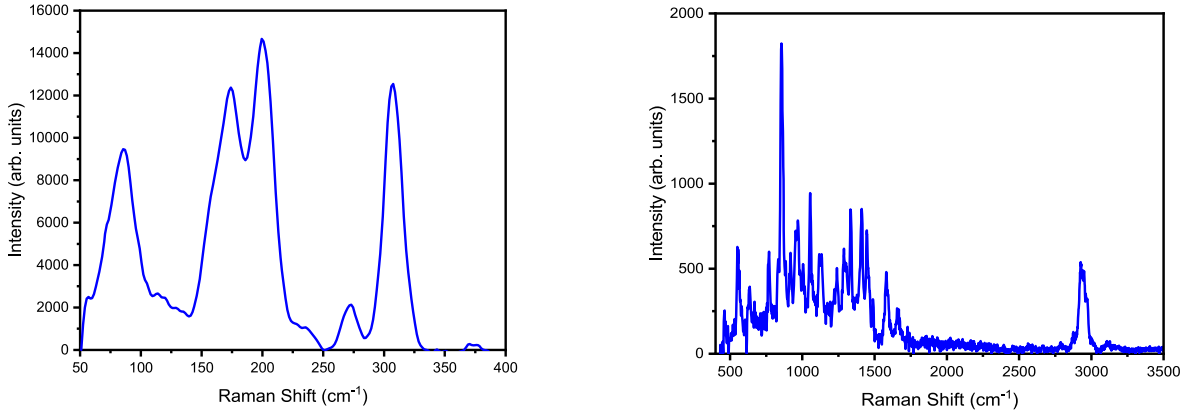

Fig. 8. Raman spectrum of $C_6H_{20}Cl_4MnN_2O_6$ obtained using a red laser with a wavelength of 786 nm at a power of 1 mW. The spectrum is shown in two ranges: (a) 50-400 cm^{-1} and (b) 400-3500 cm^{-1}. (For interpretation of the references to colour in this figure legend, the reader is referred to the Web version of this article.)

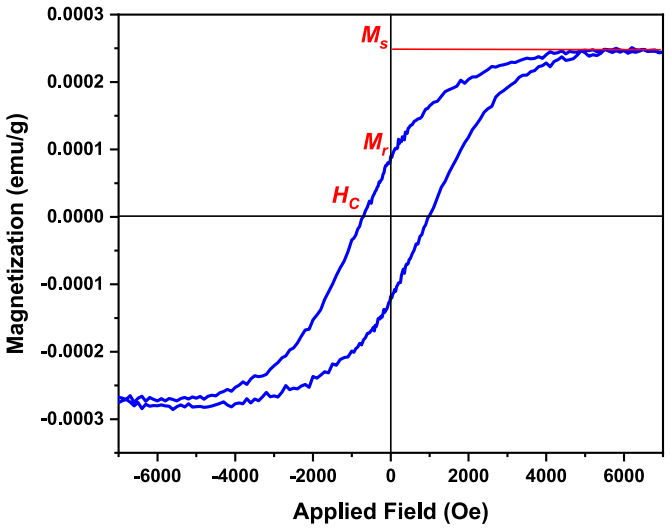

Fig. 9. Vibrating sample magnetometer hysteresis loop measurement of $C_6H_{20}Cl_4MnN_2O_6$ at room temperature.

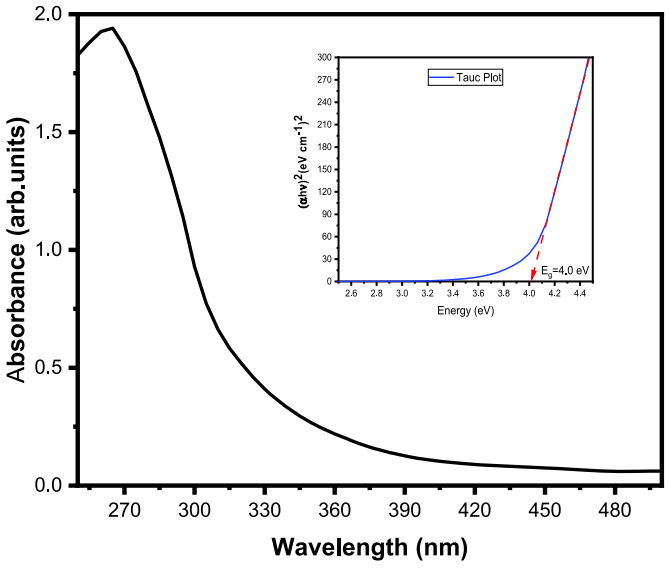

Fig. 10. Tauc plot curve analysis and UV/vis diffuse absorbance plots of $C_6H_{20}Cl_4MnN_2O_6$.

3.5. Raman analysis

Raman spectroscopy is a valuable tool for examining material structure and crystallinity. Here, we present the spectrum of $C_6H_{20}Cl_4MnN_2O_6$ crystal, obtained using a red laser with a wavelength of 785 nm and various power levels. By adjusting the power, we overcame fluorescence issues and obtained structural information for both the organic and inorganic components.

Fig. 7 displays the Raman spectra at different laser powers (1–100 mW). The intensity of each peak is power-dependent, and the highest resolution spectrum is observed at 100 mW. The spectra are divided into two frequency ranges: 50-400 cm-1 for the inorganic component and 400-3500 cm-1 for the organic component. The reference spectrum for attributing vibrational modes is obtained at 100 mW. Mode attributions are shown in Fig. 8a and b, referencing literature data [17,45–48]. Table 5 summarizes all observed vibrational bands.

In the 50-400 cm^{-1} range (Fig. 8a), the organic external and inorganic internal modes are concentrated. For example, vibrational frequencies like υs = 175 cm^{-1}, υas = 200 cm^{-1}, and υs = 87 cm^{-1} correspond to bending vibrations of the octahedral $[MnCl_4(H_2O)_2]$ moiety. Stretching modes for Mn–Cl bonds are detected at 272 and 307 cm^{-1}. Beyond 400 cm^{-1} (Fig. 8b), various vibrational features are identified. The band at 550 cm^{-1} corresponds to the stretching mode of Mn–O. Other notable vibrations include twisting modes of NH_3 groups (460, 663, 770, and 796 cm^{-1}), deformation vibrations within the plane and out of the plane of *C*–C═O and *C*–C–O, rocking mode of *C*–H (855 cm^{-1}), stretching modes of *C*–C and *O*–H (954 and 969 cm^{-1}), and *C*–C skeletal vibration (1056 cm^{-1}).

Additional frequencies include 1241, 1189, and 1336 cm^{-1} for the rocking vibration of NH_3 groups, deformation modes of *O*–H groups, and –CH_2- wagging vibration. The deformation vibration of –CH_2- is observed at 1411 cm^{-1}, while 1449 and 1489 cm^{-1} correspond to asymmetric and symmetric deformation vibrations of –CH_2- groups. The C═O stretching vibration is marked at 1580 cm^{-1}, and the frequencies 2926 and 2941 cm^{-1} represent symmetric and asymmetric stretching vibrations of the –CH_2- bond. Finally, the stretching vibration of NH_3 is situated at 2951 and 3000 cm^{-1}.

3.6. VSM magnetization curve

$C_6H_{20}Cl_4MnN_2O_6$ exhibits a distinct and robust ferromagnetic hysteresis loop with a remnant magnetization (Mr) of approximately 0.824 × 10^{-4} emu. g^{-1} and a magnetic saturation (Ms) value close to 2.48× 10^{-4} emu. g^{-1}. The coercive field (Hc), which is the reverse field required to nullify the magnetization after saturation, measures at 700 Oe. It is noteworthy that the magnetic properties of $C_6H_{20}Cl_4MnN_2O_6$ are predominantly influenced by the transition metals present in the inorganic sheet.

Refer to Fig. 9 for a visualization of the Vibrating Sample Magnetometer hysteresis loop measurement of $C_6H_{20}Cl_4MnN_2O_6$ at room temperature.

3.7. UV absorption properties

We employed a method relying on ultraviolet/visible light absorption to conduct diffuse absorbance measurements, as illustrated in Fig. 10. The compound in question, $C_6H_{20}Cl_4MnN_2O_6$, exhibited a substantial absorption edge observed at a wavelength of 325 nm, with a noticeable absence of absorption at 400 nm.

To determine the energy band gap from the UV/visible spectroscopy, we plotted (αhν)n against energy (with n values of ½ or 2) using the method known as Tauc plot. Comparing the estimated energy band gap value of 4.0 eV for our compound to that of similar compounds like $C_6H_{20}Cl_6N_2O_4Sn$ (3.5 eV) and $C_4H_{10}Cl_3NO_2Sn$ (2.85 eV). [18,19], it becomes evident that our value is notably higher. It significantly surpasses the energy gap values reported in the literature, where energy gaps around Eg = 1.2 eV are common [49].

For a visual representation, please refer to Fig. 10, showcasing the UV/vis diffuse absorbance plots and the Tauc plot curve derived from the UV/Vis analysis of $C_6H_{20}Cl_4MnN_2O_6$

4. Conclusion

In this study, we successfully determined the structure of $C_6H_{20}Cl_4MnN_2O_6$, a novel organic-inorganic hybrid compound, under ambient conditions. The structure exhibits alternating layers of inorganic and organic components stacked along the a-axis, forming a layered system. Optimization calculations using the DFT/B3LYP/LANL2MB method provided valuable insights into this compound.

Our analysis of the 3D Hirshfeld surface emphasized the crucial role of hydrogen bonds in stabilizing the structure, with prominent hydrogen interactions such as H···Cl and H···H. We carefully identified all vibrational bands by comparing their frequencies with those of similar molecules.

At room temperature, this compound displays ferromagnetic properties, including a remaining magnetization of 0.824×10^{-4} emu. g^{-1}, a coercive field close to 700 Oe, and a saturation magnetization of 2.48×10^{-4} emu. g^{-1}. Notably, the determined energy gap of 4.0 eV exceeds that of similar compounds, highlighting its unique characteristics.

These findings provide valuable insights into the structural and magnetic attributes of this intriguing organic-inorganic hybrid compound.

Authorship contributions

Category 1.

Conception and design of study: A. Kaiba, Mohammed H. Geesi

Acquisition of data: P. Guinneau, A. kaiba

Analysis and/or interpretation of data: A. Kaiba, Mohammed H. Geesi.

Category 2.

Drafting the manuscript: A. kaiba, Mohammed H. Geesi

Revising the manuscript critically for important intellectual content: All co-authors,

Category 3.

Approval of the version of the manuscript to be published (the names of all authors must be listed):

Abdellah. Kaiba, Mohammed H. Geesi, Philippe. Guionneau.

Declaration of competing interest

The authors declare that they have no known competing financial interests or personal relationships that could have appeared to influence the work reported in this paper.The authors declare the following financial interests/personal relationships which may be considered as potential competing interests:The authors whose names are listed above certify that they have no affiliations with or involvement in any organization or entity with any financial interest (such as honoraria; educational grants; participation in speakers' bureaus; membership, employment, consultancies, stock ownership, or other equity interest; and expert testimony or patent-licensing arrangements), or non-financial interest (such as personal or professional relationships, affiliations, knowledge or beliefs) in the subject matter or materials discussed in this manuscript.

Data availability

No data was used for the research described in the article.

Acknowledgment

This publication was supported by the Deanship of Scientific Research at Prince Sattam bin Abdulaziz University, Alkharj, Saudi Arabia.

Appendix A. Supplementary data

Supplementary data to this article can be found online at https://doi.org/10.1016/j.mtchem.2023.101852.

References

[1] L.N. Quan, B.P. Rand, R.H. Friend, S.G. Mhaisalkar, T.-W. Lee, E.H.J.C.r. Sargent, Perovskites for next-generation optical sources, Chem. Rev. 119 (2019) 7444–7477.

[2] J. Niederhausen, K.A. Mazzio, R.W.J.E.S. MacQueen, Inorganic–organic interfaces in hybrid solar cells, Electron. Struct. 3 (2021), 033002.

[3] L. Jonathan, L.J. Diguna, O. Samy, M. Muqoyyanah, S. Abu Bakar, M. D. Birowosuto, A.J.P. El Moutaouakil, Hybrid organic–inorganic perovskite halide materials for photovoltaics towards their commercialization, Polymers 14 (2022) 1059.

[4] D.B. Mitzi, K. Chondroudis, C.R. Kagan, development, Organic-inorganic electronics, IBM J. Res. Dev. 45 (2001) 29–45.

[5] R. Otero, A.V. de Parga, J.M. Gallego, Electronic, structural and chemical effects of charge-transfer at organic/inorganic interfaces, Surf. Sci. Rep. 72 (2017) 105–145.

[6] J. Muñoz, E. Redondo, M.J.S. Pumera, Versatile design of functional organic–inorganic 3D-printed (opto) electronic interfaces with custom catalytic activity, Small 17 (2021), 2103189.

[7] D.B. Mitzi, Synthesis, crystal structure, and optical and thermal properties of (C4H9NH3) 2MI4 (M= Ge, Sn, Pb), Chem. Mater. 8 (1996) 791–800.

[8] M. Essid, M. Rzaigui, H. Marouani, Synthesis, characterization and antioxidant activity of a novel organic–inorganic hybrid material trans-2, 5-dimethylpiperazine-1, 4-diium pentachlorobismuthate (III):[C6H16N2] BiCl5, J. Mol. Struct. 1117 (2016) 257–264.

[9] N.L. Allan, M.J. Dayer, D.T. Kulp, W.C. Mackrodt, Atomistic Lattice Simulations of the Ternary Fluorides AMF3 (A= Li, Na, K, Rb, Cs; M= Mg, Ca, Sr, Ba), vol. 1, 1991, pp. 1035–1039.

[10] G.C. Papavassiliou, Three-and low-dimensional inorganic semiconductors, Prog. Solid State Chem. 25 (1997) 125–270.

[11] T. Kataoka, T. Kondo, R. Ito, S. Sasaki, K. Uchida, N.J.P.R.B. Miura, Magneto-optical study on excitonic spectra in (C 6 H 13 NH 3) 2 PbI 4, Phys. Rev. B 47 (1993) 2010.

[12] W. Bi, N. Louvain, N. Mercier, J. Luc, I. Rau, F. Kajzar, B.J.A.M. Sahraoui, A switchable NLO organic-inorganic compound based on conformationally chiral disulfide molecules and Bi (III) I5 iodobismuthate networks, Adv. Mater. 20 (2008) 1013–1017.

[13] N. Louvain, N. Mercier, F.J.I.C. Boucher, α-to β-(dmes) BiI5 (dmes= dimethyl (2-ethylammonium) sulfonium dication): umbrella reversal of sulfonium in the solid state and short I I interchain contacts. Crystal structures, optical properties, and theoretical investigations of 1D iodobismuthates, Inorg. Chem. 48 (2009) 879–888.

[14] S.H. Mir, L.A. Nagahara, T. Thundat, P. Mokarian-Tabari, H. Furukawa, A. Khosla, Organic-inorganic hybrid functional materials, Integr. Platform Appl. Technol. 165 (2018) B3137–B3156.

[15] K. Liao, X. Hu, Y. Cheng, Z. Yu, Y. Xue, Y. Chen, Q. Gong, Spintronics of hybrid organic–inorganic perovskites: miraculous basis of integrated optoelectronic devices, Adv. Opt. Mater. 7 (2019), 1900350.

[16] G. Breneman, R. Willett, C. Chemistry, Diethylenetriammonium tetrachloromanganate (II) chloride, Acta Crystallogr. B Struct. Crystallogr. Cryst. Chem. 37 (1981) 1292–1294.

[17] M.B. AlShammari, A. Kaiba, P. Guionneau, M.H. Geesi, T. Aljohani, Y.J.C.P. L. Riadi, Phase transitions, optical and electronic properties of the layered perovskite hybrid [NH3 (CH2) 2COOH] 2CdCl4 of Y-aminobutyric acid (GABA), Chem. Phys. Lett. 702 (2018) 8–15.

[18] A. Kaiba, M.H. Geesi, P.J.P. Guionneau, A New Organic–Inorganic Hybrid Compound: synthesis, crystal structure, Hirshfeld surface analysis, vibrational, optical, magnetic properties and theoretical study, Polyhedron 217 (2022), 115717.

[19] A. Kaiba, F. Al Otaibi, M.H. Geesi, Y. Riadi, T.A. Aljohani, P. Guionneau, A new organic–inorganic hybrid compound (NH3 (CH2) C6H4CO2H)[SnCl6]: synthesis, crystal structure, vibrational, optical, magnetic properties and theoretical study, J. Mol. Struct. 1234 (2021), 130129.

[20] S. Gatfaoui, H. Dhaouadi, T. Roisnel, M. Rzaigui, H. Marouani, m-Xylylenediaminium dinitrate, Acta Crystallogr., Sect. E: Struct. Rep. Online 70 (2014) o398–o399.

[21] M.M. Lee, J. Teuscher, T. Miyasaka, T.N. Murakami, H.J.J.S. Snaith, Efficient hybrid solar cells based on meso-superstructured organometal halide perovskites, Science 338 (2012) 643–647.

[22] G. Xing, N. Mathews, S. Sun, S.S. Lim, Y.M. Lam, M. Grätzel, S. Mhaisalkar, T.C.J. S. Sum, Long-range balanced electron-and hole-transport lengths in organic-inorganic CH3NH3PbI3, Science 342 (2013) 344–347.

[23] H. Zhou, Q. Chen, G. Li, S. Luo, T.-b. Song, H.-S. Duan, Z. Hong, J. You, Y. Liu, Y.J. S. Yang, Interface engineering of highly efficient perovskite solar cells, Science 345 (2014) 542–546.

[24] C. Aruta, F. Licci, A. Zappettini, F. Bolzoni, F. Rastelli, P. Ferro, T.J.A.P.A. Besagni, Growth and optical, magnetic and transport properties of (C4H9NH3) 2MCl4 organic-inorganic hybrid films (M= Cu, Sn), Appl. Phys. A 81 (2005) 963–968.

[25] M. Wright, A.J.S.e.m. Uddin, s. cells, Organic—inorganic hybrid solar cells, A Comparative Rev. 107 (2012) 87–111.

[26] C.-F. Lin, W.-F. Su, C.-I. Wu, I.-C. Cheng, Organic, Inorganic and Hybrid Solar Cells: Principles and Practice, John Wiley & Sons, 2012.

[27] Y. Zhao, K.J.C.S.R. Zhu, Organic–inorganic hybrid lead halide perovskites for optoelectronic and electronic applications, Chem. Soc. Rev. 45 (2016) 655–689.

[28] U. Khan, Y. Zhinong, A.A. Khan, A.J.S.E. Zulfiqar, Organic–inorganic hybrid perovskites based on methylamine lead halide solar cell, Sol. Energy 189 (2019) 421–425.

[29] Z. Yi, N.H. Ladi, X. Shai, H. Li, Y. Shen, M.J.N.A. Wang, Will organic–inorganic hybrid halide lead perovskites be eliminated from optoelectronic applications? Nanoscale Adv. 1 (2019) 1276–1289.

[30] C.J.F.i.c. Lin, Stabilizing organic–inorganic lead halide perovskite solar cells with efficiency beyond 20, Front. Chem. 8 (2020) 592.

[31] A. Altomare, M.C. Burla, M. Camalli, G.L. Cascarano, C. Giacovazzo, A. Guagliardi, A.G. Moliterni, G. Polidori, R. Spagna, SIR97: a new tool for crystal structure determination and refinement, J. Appl. Crystallogr. 32 (1999) 115–119.

[32] G. Sheldrick, SHELXL-97 (Release 97-2, University of Göttingen, Germany, 1998.

[33] L.J. Farrugia, WinGX and ORTEP for windows: an update, J. Appl. Crystallogr. 45 (2012) 849–854.

[34] C.F. Macrae, I.J. Bruno, J.A. Chisholm, P.R. Edgington, P. McCabe, E. Pidcock, L. Rodriguez-Monge, R. Taylor, J. Streek, P.A. Wood, Mercury CSD 2.0–new features for the visualization and investigation of crystal structures, J. Appl. Crystallogr. 41 (2008) 466–470.
[35] P.J.D.T. Guionneau, Crystallography and spin-crossover. A view of breathing materials, Dalton Trans. 43 (2014) 382–393.
[36] M. Frisch, G. Trucks, H. Schlegel, G. Scuseria, M. Robb, J. Cheeseman, G. Scalmani, V. Barone, G. Petersson, H. Nakatsuji, Gaussian 16, Revision C. 01, Gaussian, Inc, Wallingford, 2016.
[37] A. Becke, Density-functional thermochemistry. III. The role of exact exchange, J. Chem. Phys. 98 (1993) 5648.
[38] R. Parr, W. Yang, Density Functional Theory of Atoms and Moleculesoxford Univ, Press, New York, 1989.
[39] C. Lee, W. Yang, R.G. Parr, Development of the Colle-Salvetti correlation-energy formula into a functional of the electron density, Phys. Rev. B 37 (1988) 785.
[40] P.J. Stephens, F.J. Devlin, C.F. Chabalowski, M.J. Frisch, Ab initio calculation of vibrational absorption and circular dichroism spectra using density functional force fields, J. Phys. Chem. 98 (1994) 11623–11627.
[41] P.J. Hay, W.R. Wadt, Ab initio effective core potentials for molecular calculations. Potentials for the transition metal atoms Sc to Hg, J. Chem. Phys. 82 (1985) 270–283.
[42] M. Essid, S. Muhammad, H. Marouani, A. Saeed, Z. Aloui, A. Al-Sehemi, Synthesis, characterization, Hirshfeld surface analysis and computational studies of 1-methylpiperazine-1, 4-diium bis (hydrogen oxalate):[C5H14N2](HC2O4) 2, J. Mol. Struct. 1211 (2020), 128075.
[43] GaussView, Version 6.1.1, Roy Dennington, Todd Keith, and John Millam, Semichem Inc., Shawnee Mission, KS, 2019.
[44] M. Turner, J. McKinnon, S. Wolff, D. Grimwood, P. Spackman, D. Jayatilaka, M. Spackman, CrystalExplorer. Version 17, University of Western Australia, 2017.
[45] C. Han, D.B. Cordes, A.M. Slawin, P.J.C. Lightfoot, Structural variations in manganese halide chain compounds mediated by methylimidazolium isomers, Crystals 10 (2020) 930.
[46] S. Hassen, H. Chebbi, M.F. Zid, Y. Arfaoui, Synthesis of [MnCl3 (H2O) 2 (Hatz)] H2O and investigation of its structure via X-ray diffraction, spectroscopic measurements and DFT calculations, J. Iran. Chem. Soc. 15 (2018) 2659–2668.
[47] A. Kaiba, M.H. Geesi, P. Guionneau, T.A. Aljohani, L. Bih, H. Bih, S. Kassou, Synthesis, Structural and Raman Spectroscopic in Organic– Inorganic Halide Perovskites Based on β-Alanine, vol. 1204, 2020, 127380.
[48] I. Dhouib, A. Ouasri, Z. Elaoud, Disordered structures, vibrational spectroscopy, thermal behavior, and electrical properties of two new tetrachlorometallates complexes [(CH3CH2CH2) 4N] 2MIICl4 with MII= Co and Mn, J. Saudi Chem. Soc. 24 (2020) 567–583.
[49] K. Shen, H.L. Sun, G. Ji, Y. Yang, Z. Jiang, F.J.N. Song, Fabrication and Characterization of Organic–Inorganic Hybrid Perovskite Devices with External Doping, Nanoelectronics and Materials Development, 2016, p. 95.